Faraday Discussions

Photoresponsive Frameworks: Energy Transfer in the Spotlight

Journal:	*Faraday Discussions*
Manuscript ID	FD-ART-02-2021-000013.R1
Article Type:	Paper
Date Submitted by the Author:	08-Apr-2021
Complete List of Authors:	Martin, Corey; University of South Carolina, Department of Chemistry and Biochemistry Park, Kyoung Chul; University of South Carolina, Department of Chemistry and Biochemistry Corkill, Ryan; University of South Carolina, Department of Chemistry and Biochemistry Kittikhunnatham, Preecha; University of South Carolina, Chemistry and Biochemistry Leith, Gabrielle; University of South Carolina, Department of Chemistry and Biochemistry Mathur, Abhijai; University of South Carolina, Department of Chemistry and Biochemistry Abiodun, Sakiru; University of South Carolina, Department of Chemistry and Biochemistry Greytak, Andrew; University of South Carolina, Department of Chemistry and Biochemistry Shustova, Natalia; University of South Carolina, Department of Chemistry and Biochemistry

PAPER

Photoresponsive Frameworks: Energy Transfer in the Spotlight

Corey R. Martin,[a] Kyoung Chul Park,[a] Ryan E. Corkill,[a] Preecha Kittikhunnatham,[a] Gabrielle A. Leith,[a] Abhijai Mathur,[a] Sakiru L. Abiodun,[a] Andrew B. Greytak,[a] and Natalia B. Shustova*[a]

Received 00th January 20xx, Accepted 00th January 20xx

DOI: 10.1039/x0xx00000x

In this paper, spiropyran-containing metal- and covalent-organic frameworks (MOFs and COFs, respectively) are probed as platforms for fostering photochromic behavior in solid-state materials while simultaneously promoting directional energy transfer (ET). In particular, Förster resonance energy transfer (FRET) between spiropyran and porphyrin derivatives integrated as linkers in the framework matrix is discussed. The photochromic spiropyran derivatives allows for control over material optoelectronic properties through alternation of excitation wavelengths. Photoinduced changes in the material electronic profile have also been probed through conductivity measurements. Time-resolved photoluminescence studies were employed to evaluate the effect of photochromic linkers on material photophysics. Furthermore, “forward” and “reverse” FRET processes occurring between two distinct chromophores were modeled, and the Förster critical radii and ET rates were estimated to support the experimentally observed changes in material photoluminescence.

Introduction

Mimics of the natural photosystem, that rely on the spatial organization of hundreds of thousands of porphyrinoid derivatives (capable of, for example, oxygen transport in hemoglobin or detoxification of anthropogenics via cytochrome P450), have been central to research thrusts due to their proven and unrivalled potentials.[1–3] Crystalline metal- or covalent-organic frameworks (MOFs and COFs, respectively) could promote hierarchical organization of organic linkers that can be assembled around metal centers,[4–25] opening a pathway for scaffold-imposed photocatalysis. Such chromophore organization through COFs or MOFs presents an opportunity to study and model energy transfer (ET) processes for realization of directional ET in frameworks.[26–28] There are a number of studies focused on ET processes in MOFs[27–35] and COFs[36,37] that describe different mechanisms and methods to achieve efficient ET. Herein, we consider the possibility to modulate the ET processes, in

[a] Department of Chemistry and Biochemistry, University of South Carolina, Columbia, 631 Sumter Street, South Carolina 29208, USA. E-mail: shustova@sc.edu

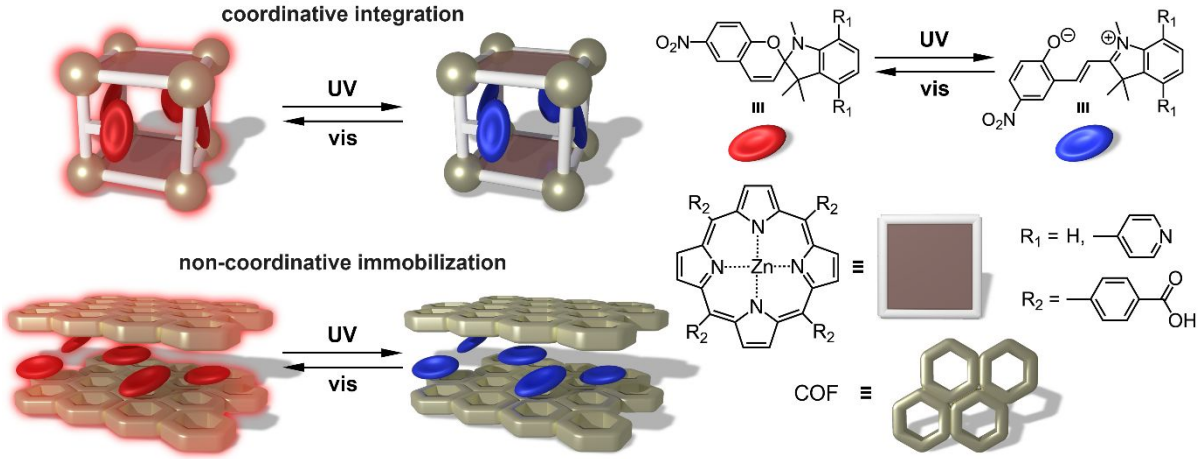

Scheme 1. (*top left*) Schematic representation of photoresponsive MOFs containing photochromic spiropyran moieties coordinatively immobilized inside a framework. (*bottom left*) Spiropyran derivatives integrated as guests inside a COF through non-coordinative immobilization. (*right*) The components for MOF and COF preparation including the photoisomerization of the spiropyran core under UV and visible excitations.

particular Förster resonance energy transfer (FRET), through spiropyran-based photochromic units embedded in the rigid matrix of a framework as either a side group or a guest (Scheme 1). The prepared materials were studied by powder and single-crystal X-ray diffraction (PXRD and SC-XRD, respectively), ^{1}H nuclear magnetic resonance (NMR) spectroscopy, mass-spectrometry (MS), and conductivity measurements as well as diffuse reflectance, steady-state, and time-resolved photoluminescence (PL) spectroscopy; the latter spectroscopic techniques were employed to study the possibility of directing excited-state decay pathways through photoisomerization of a spiropyran moiety integrated inside a rigid framework.

Results and discussion

Spiropyran and its derivatives exhibit rapid photoinduced spiropyran-to-merocyanine isomerization in solution;[38–40] however, in the solid-state, similar transformations are hindered due to significant structural rearrangements accompanied with photoisomer conversion.[40] Recent progress in the field of spiropyran-based materials has demonstrated that MOFs can serve as a platform to promote such transformations in the solid state by providing framework voids for spiropyran photoisomerization to occur in.[41–44] Remarkably, it was demonstrated that such MOF-promoted photoisomerization can occur with rates comparable to those in solution.[42] In contrast to the previously reported diarylethene-based MOFs, another common class of photochromic molecule[45,46] that has been integrated as a part of a framework skeleton (i.e., coordinated to the metal from both sides of a diarylethene core),[31,32,47–49] spiropyran photoisomerization occurs inside of the framework pores. Consequently, the rearrangement of a photochromic unit is less sterically hindered, that is reflected by the photoisomerization rates.[42]

For integration within a MOF, we synthesized a photochromic spiropyran-based derivative, 1',3',3'-trimethyl-6-nitro-4',7'-di(pyridin-4-yl)spiro[chromene-2,2'-indoline]

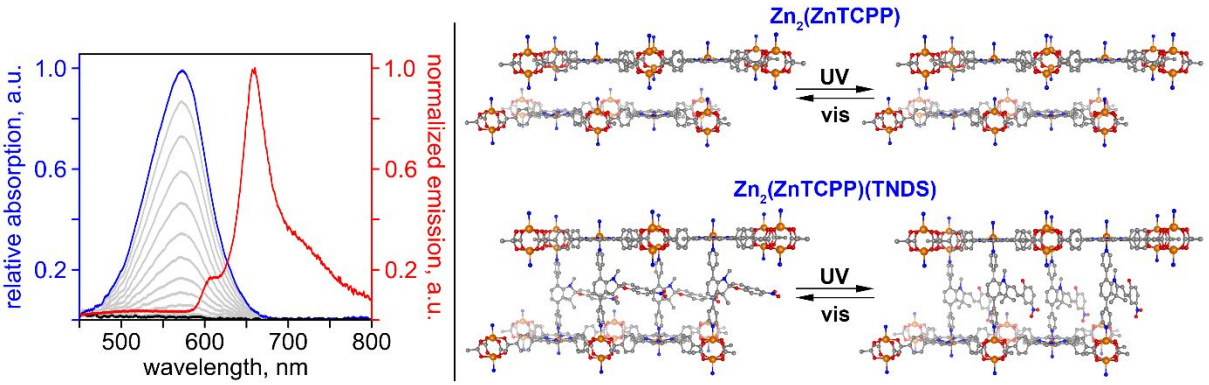

Figure 1. (*left*) Normalized absorption spectra of TNDS (63 μM in DMF) in the open (blue trace) and closed (black trace) forms. The gray lines correspond to the absorption spectra of TNDS collected during conversion from open to closed forms. The red trace shows the normalized solid-state emission spectrum of Zn_2(ZnTCPP) (λ_{ex} = 350 nm). (*right*) Structures of (*top*) Zn_2(ZnTCPP) and (*bottom*) Zn_2(ZnTCPP)(TNDS).

(TNDS), functionalized with two pyridyl arms for coordination to a metal center.[42] A framework for TNDS integration was selected based on two criteria: the presence of metal sites available for coordination of the photochromic linker and an appropriate spectral overlap of the donor (D) emission and acceptor (A) absorption spectra that is required for FRET to take place.[27,28] Both of these criteria are satisfied by the two-dimensional (2D) framework, Zn_2(ZnTCPP) (H_4TCPP = tetrakis(4-carboxyphenyl)-porphyrin).[50] This framework is composed of 2D layers consisting of paddlewheel $Zn_2(O_2C–)_4$ secondary-building units (SBUs), bridged together by $ZnTCPP^{4-}$ ligands (Figure 1).[50] In the paddlewheel-based SBUs of Zn_2(ZnTCPP), Zn atoms are axially coordinated with labile solvent molecules that can be replaced by TNDS, resulting in the coordinative integration of photochromic pillars between porphyrin-based layers and construction of a three-dimensional (3D) photoresponsive framework (Figure 1).[51,52] In Figure 1, it is shown that the porphyrin-containing 2D framework emits at $\lambda_{em(max)}$ = 660 nm (λ_{ex} = 350 nm), and its emission spectrum overlaps with the TNDS absorption profile. Due to the spectral overlap and photoinduced control of the TNDS absorption profile, we hypothesized that TNDS photoisomerization could result in changes of the MOF emission profile and modulate resonance ET efficiency. However, TNDS emission ($\lambda_{em(max)}$ = 690 nm; λ_{ex} = 350 nm) also overlaps with absorption of Zn_2(ZnTCPP) (Figure S1), and therefore, the "reverse" process of transferring energy from TNDS to Zn_2(ZnTCPP) could also take place. Therefore, there could be two pathways for FRET to occur: from Zn_2(ZnTCPP) (D) to TNDS (A), that will be referred to from now on as a "forward" FRET process and from TNDS (D) to Zn_2(ZnTCPP) (A; "reverse" FRET).

Heating of TNDS in the presence of $Zn(NO_3)_2{\cdot}6H_2O$ and H_4TCPP in a *N*,*N*-diethylformamide/ethanol/nitric acid mixture at 80 °C for 14 h led to the formation of dark-red crystals of Zn_2(ZnTCPP)(TNDS). According to PXRD data, novel Zn_2(ZnTCPP)(TNDS) is isostructural to Zn_2(DBTD)(TNDS) (H_4DBTD = 3′,6′-dibromo-4′,5′-bis(4-carboxyphenyl)-[1,1′:2′,1″-terphenyl]-4,4″-dicarboxylic acid), also containing photochromic TNDS (Figure S2).[42] Similar to Zn_2(DBTD)(TNDS),[42] the 2D layers of Zn_2(ZnTCPP) are connected by TNDS pillars. These structural similarities are reflected by the resemblance in PXRD patterns of Zn_2(ZnTCPP)(TNDS) and Zn_2(DBTD)(TNDS)[42] as shown in Figure S2. Crystals of

Zn_2(ZnTCPP)(TNDS) were sufficient to perform SC-XRD analysis; however, due to significant crystallographic disorder (likely occurring due to the rotational and photoresponsive nature of the coordinated TNDS linker), anisotropic refinement could not be performed for all atoms in the structure, even upon utilization of synchrotron radiation. This challenge is common for porphyrin-based photochromic frameworks,[31,32] and the situation becomes even more complex due to the presence of the photochromic unit isomerizing under irradiation.[53,54] The collected unit cell parameters of Zn_2(ZnTCPP)(TNDS), $a = b = 16.642$ Å, and $c = 34.002$ Å ($\alpha = \beta = \gamma = 90°$), are distinct from those of 2D Zn_2(ZnTCPP) by the unit cell parameter, c. This parameter indicates a change of the interlayer distance from 34 Å (Zn_2(ZnTCPP)(TNDS)) to 19 Å[50] (Zn_2(ZnTCPP)). This interlayer expansion is consistent with the length of TNDS (11.416 Å, measured as the N···N distance between pyridyl arms of TNDS). Comparison of the PXRD patterns of Zn_2(ZnTCPP)(TNDS) and Zn_2(ZnTCPP)[42,50] revealed a peak shift from higher 2θ to lower angles, that is also associated with the interlayer expansion observed in Zn_2(ZnTCPP)(TNDS) (e.g., from $2\theta = 9.6°$ (002) in the Zn_2(ZnTCPP) pattern to $2\theta = 4.9°$ (002) in the Zn_2(ZnTCPP)(TNDS) pattern). Integration of TNDS between 2D porphyrin-based layers was also confirmed by Fourier-transform infrared (FTIR) spectroscopy through the appearance of the ν(C–O–C) stretch associated with presence of the benzopyran group in the TNDS linker (its absence was also confirmed in Zn_2(ZnTCPP), Figure S3).[55] According to ^{1}H NMR spectroscopy and MS of the digested Zn_2(ZnTCPP)(TNDS) sample (Figure S4), H_4TCPP and TNDS are present in a ratio of 1 : 0.98, indicating almost complete installation of photochromic TNDS between the Zn_2(ZnTCPP) layers.

To confirm that embedded TNDS preserves its photochromic behavior upon immobilization inside a MOF's rigid matrix, the spectroscopic properties of Zn_2(ZnTCPP)(TNDS) were studied under irradiation with UV and visible light. The changes in absorption profile were monitored by time-resolved diffuse reflectance spectroscopy (Figure 2). The attenuation rate for the TNDS cyclization reaction (merocyanine-to-spiropyran) immobilized in Zn_2(ZnTCPP)(TNDS) was estimated under visible-light irradiation (a 400-nm longpass filter was used to remove UV light from a white halogen lamp) and was found to be 1.5×10^{-1} s^{-1}, which is in line with the previously reported value for Zn_2(DBTD)(TNDS) (1.6×10^{-1} s^{-1}).[42] Therefore, TNDS integrated in the matrix of the porphyrin-based MOF still exhibited photochromic behavior. Moreover, the estimated cyclization rate of Zn_2(ZnTCPP)(TNDS) is comparable with the photoisomerization rate of TNDS in a 3 mM *N*,*N*-dimethylformamide (DMF) solution (1.2×10^{-1} s^{-1}).[42] A detailed description of photophysical experiments is given in the Experimental Section below.

As previously described, switching of spiropyran from its "closed" form to its zwitterionic photoisomer (merocyanine) induces a change in conjugation and charge distribution.[40,45,56–60] The difference in electronic structure of photoisomers gives rise to the possibility of current cycling (i.e., changes in current values with a steady applied bias (500 mV)) upon irradiation alternation (i.e., switching between 365-nm and 590-nm excitation) as shown in Figure 2. Furthermore, the time-resolved changes observed optically in the diffuse reflectance profile closely match the changes in the electronic properties (Figure 2). To demonstrate that the observed changes were exclusively associated with the installed photochromic linker, TNDS, control experiments using non-photochromic Zn_2(ZnTCPP) were carried out. Indeed, no optical or current cycling was observed for non-photochromic Zn_2(ZnTCPP), as shown in Figure 2.

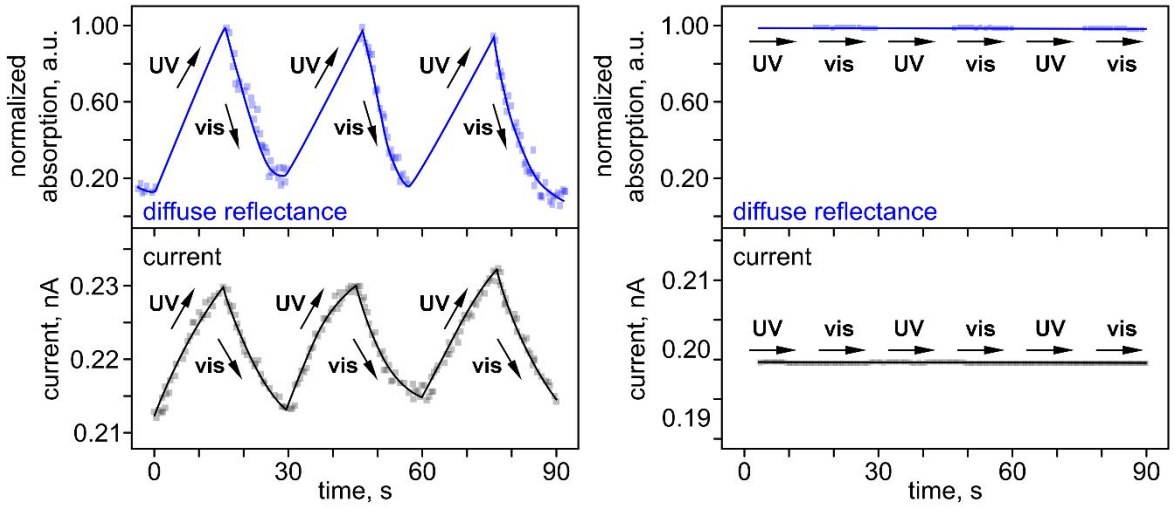

Figure 2. (*left*) Normalized optical and current cycling of photochromic Zn_2(ZnTCPP)(TNDS) through alternation of UV (λ_{ex} = 365 nm) and visible (λ_{ex} = 590 nm) irradiation. (*right*) Control experiments performed for Zn_2(ZnTCPP) under alternation of UV (λ_{ex} = 365 nm) and visible (λ_{ex} = 590 nm) irradiation. Absorption of the UV-irradiated sample is normalized to a value of 1.0 at 665 nm and all subsequent values are scaled according to this value.

Moreover, changes in the absorption edge of Zn_2(ZnTCPP)(TNDS) upon UV-light excitation is consistent with a reduction in band gap (Figure S5).[43,60–62] The possibility of the "forward" FRET process between Zn_2(ZnTCPP) (D) and TNDS (A) was evaluated through steady-state and time-resolved PL studies. The Zn_2(ZnTCPP) framework (Figure 1) possesses a broad emission in the range of 600–750 nm with λ_{max} = 650 nm (λ_{ex} = 350 nm). If only the "forward" FRET process took place (in the absence of "reverse" FRET), changes in the absorption profile associated with spiropyran-to-merocyanine conversion would result in a dramatic alteration of the PL spectrum due to quenching of Zn_2(ZnTCPP) emission (and enhancement of TNDS emission), as the D-A distance is well below the Förster critical transfer radius (*vide infra*). Indeed, Figure 3 clearly shows changes in the emission profile of Zn_2(ZnTCPP)(TNDS), resulting in an overall decrease in intensity after 90-s of *in situ* irradiation with UV light (λ_{ex} = 330–385 nm) by 47%. Restoration of Zn_2(ZnTCPP)(TNDS) emission was observed upon sample irradiation with 590-nm light (or, over time in the dark). Control experiments performed on non-photochromic Zn_2(ZnTCPP) demonstrated the absence of emission alternation (Figure 3), providing further confirmation that optical cycling was observed due to the presence of photoresponsive linkers. Time-resolved PL data indicated a shorter decay lifetime for Zn_2(ZnTCPP)(TNDS) compared to that of Zn_2(ZnTCPP) (Figure S6). Analysis of the obtained curves revealed multiexponential decay in each case (supporting fits are described in Table S1). As a result of the analysis, shortening of the amplitude-averaged lifetime (τ) from 0.893 ns (Zn_2(ZnTCPP)) to 0.502 ns (Zn_2(ZnTCPP)(TNDS)) was observed, and in the absence of the "reverse" FRET process, the corresponding "forward" FRET efficiency and ET rate would be 44% and 0.872 ns^{-1}, respectively. It is important to note, however, that the "reverse" FRET process should be considered as well. To examine the rates of "forward" and "reverse" FRET processes, we calculated the spectral overlap functions, (J), between donor and acceptor (Figure 4),

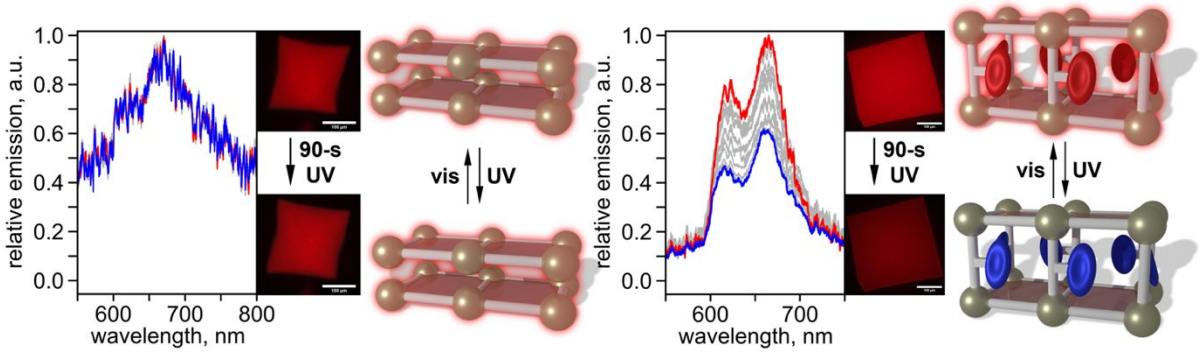

Figure 3. Emission photoswitch attenuation via epifluorescence microscopy for (*left*) Zn_2(ZnTCPP) and (*right*) Zn_2(ZnTCPP)(TNDS). Emission data of the pre-UV-irradiated samples (red) are normalized to a value of 1.0 at 665 nm and all subsequent values are scaled according to these values. The images near each plot show the epifluorescent images of single-crystals before and after 90-s UV irradiation (λ_{ex} = 330–385 nm). Schematic representation and structures of (*left*) Zn_2(ZnTCPP) and (*right*) Zn_2(ZnTCPP)(TNDS).

based on the normalized emission spectrum, approximate quantum yield, and approximate molar extinction spectrum for each species (more details can be found in the Supporting Information). Our calculations determined that $J_{\text{forward}} = 2.58 \times 10^{-14}$ M^{-1} cm^3 and $J_{\text{reverse}} = 11.2 \times 10^{-14}$ M^{-1} cm^3. The corresponding Förster critical radii (R_o) were found to be 27.3 Å ($R_{o\ \text{forward}}$) and 24.4 Å ($R_{o\ \text{reverse}}$), both of which are far greater than the D-A distance approximated from the structural data (~12 Å). Therefore, both "forward" and "reverse" FRET processes are expected to occur in our system. To predict the relative decrease in emission intensity upon UV excitation for Zn_2(ZnTCPP)(TNDS), we considered the radiative decay rate, k_r, non-radiative decay rate, k_{nr}, and ET rate, $k_{ET} = \frac{B \times J}{r^6} k_r$, (for the Zn_2(ZnTCPP) and TNDS components; B = a constant related to the refractive index and mutual orientation of chromophores, r = the distance between chromophores (estimated as 12 Å), and k_r and k_{nr} are estimated from the amplitude-average lifetime and estimated quantum yield (QY = 10% for Zn_2(ZnTCPP) and 1% for Zn_2(TNDS)(DBTD)) see the Supporting Information for more details). As a result of the performed analysis, $k_{ET\ \text{forward}}$ was estimated to be 156 ns^{-1} while $k_{ET\ \text{reverse}}$ was calculated to be 66 ns^{-1}. The kinetic model predicts limited quenching of the donor in this case, with donor emission continuing to dominate the emission spectrum due to the low radiative rate and QY of the acceptor, TNDS (in the merocyanine form; Figure 3).

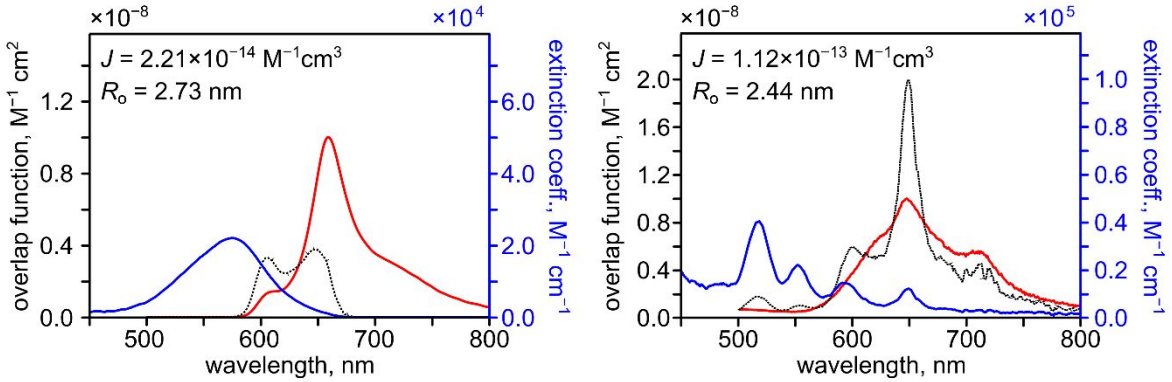

Figure 4. (*left*) Förster analysis for the forward ET process illustrating the spectral overlap function (dashed black line, left vertical axis) calculated for the measured emission spectrum of Zn_2(ZnTCPP) (red line, arbitrary scale), and the molar extinction spectrum of TNDS in DMF (63 µM, blue line, right vertical axis). (*right*) Förster analysis for the "reverse" ET process illustrating the spectral overlap function (dashed black line, left vertical axis) calculated for the measured emission spectrum of TNDS in DMF (63 µM, red line, arbitrary scale), and the molar extinction spectrum of H_4TCPP in DMF (7.8 µM, blue line, right vertical axis).

For comparison with our findings in MOFs, we probed the photochromic behavior of spiropyran integrated inside the COF as an alternative platform.[63–65] We prepared a COF (herein referred to as COF**1**) through a condensation reaction of 1,3,5-tri-(4-aminophenyl)benzene (TAPB), 2,5-dimethoxyterephthalaldehyde (DMTA), and 2,5-bis(2-propynyloxy)terephthalaldehyde (BPTA)[66,67] as shown in Figure 5. The alkyne-functionalized COF was chosen due its broad emission profile that led to sufficient spectral overlap with SP (Figure 5). The PXRD patterns and FTIR spectrum of COF**1** can be found in Figures S7 and S8, respectively. Synthesized COF**1** exhibited emission in the 500–800 nm range with $\lambda_{em(max)}$ = 680 nm (λ_{ex} = 350 nm), similar to that of Zn_2(ZnTCPP) (Figures 1 and 5). As a next step, we incorporated spiropyran, 1',3'-dihydro-1',3',3'-trimethyl-6-nitrospiro[2*H*-1-benzopyran-2,2'-(2*H*)-indole] (SP, Scheme 1) as a guest within the pores of COF**1** through 72-hr of soaking in a tetrahydrofuran (THF) solution at 40 °C, resulting in SP@COF**1** (more details are given in the Experimental section below). The amount of SP integrated into SP@COF**1** was confirmed through ^{1}H NMR spectroscopy of the digested sample (Figure S9, see the Experimental Section

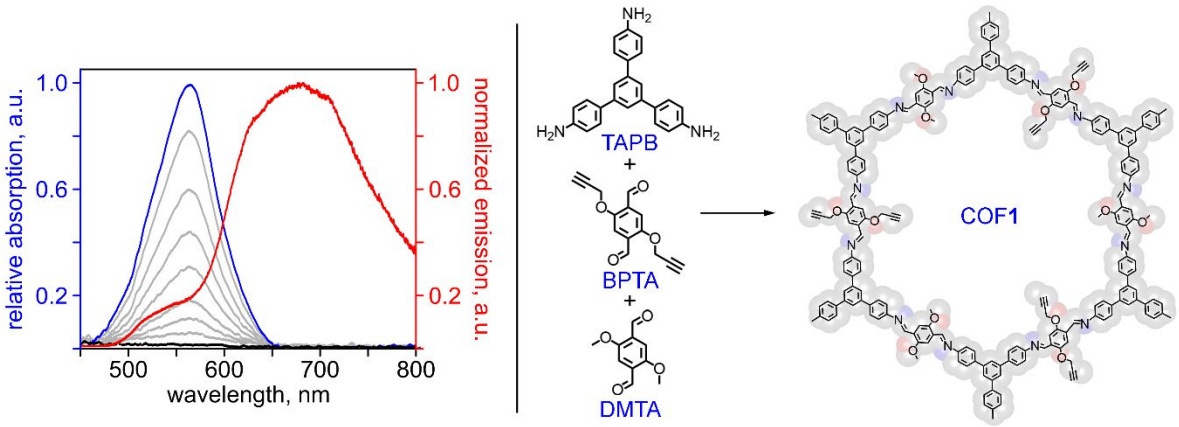

Figure 5. (*left*) Absorption spectra of SP (63 µM in DMF) in the open (blue trace) and closed (black trace) forms. The gray lines correspond to absorption spectra of SP collected during conversion from open to closed forms. The red trace shows the normalized solid-state emission spectrum of COF**1** (λ_{ex} = 350 nm). (*right*) Synthetic scheme for COF**1** and a schematic representation of its structure.

for more details). The absorption spectrum of SP is shown in Figure 5 along with the emission spectrum of COF**1**. Through analysis of the ^{1}H NMR spectrum (Figure S9), we determined that there is an average of one SP molecule per two COF pores. In a similar vein to the aforementioned studies on MOFs, we monitored changes in the emission profile of SP@COF**1** through epifluorescence measurements and, similar to Zn_2(ZnTCPP)(TNDS), emission decreased upon UV excitation (λ_{ex} = 330–385 nm, Figure S10). As expected, the control experiment performed on the parent COF**1** sample did not demonstrate changes in its emission profile (Figure S10). Therefore, we attribute the changes in SP@COF**1** to the integrated SP moiety. Furthermore, time-resolved PL measurements revealed a shortened amplitude-averaged lifetime for SP@COF**1** (0.479 ns) compared to COF**1** (0.649 ns, Figure S11). As a result, it is plausible to suggest that COFs, similar to MOFs, could be used as a platform to promote FRET processes that involve SP derivatives. A more detailed analysis of multiple-chromophore photophysics is underway.

Conclusions

The aforementioned results demonstrate that spiropyran and its derivatives integrated inside porous matrices such as COFs and MOFs maintain a photochromic response that can address the challenge for preparation of spiropyran-containing solid-state materials that has previously been encountered. Along these lines, the observed cyclization rate of synthesized TNDS is comparable with that of spiropyran derivatives in solution, only recently being achieved.[42] The photochromic behavior of TNDS was used to control the optoelectronic properties of the material through alternation of excitation wavelengths. Furthermore, "forward" and “reverse” FRET processes occurring between two types of chromophores were modeled with an estimation of Förster critical radii and energy transfer rates, confirming the experimentally observed changes in material emission intensity. The presented studies bring energy transfer of porous materials into the spotlight for developing a new generation of stimuli-responsive devices.

Experimental

Materials

Tin(II) chloride anhydrous (98%, BeanTown Chemical), copper(I) chloride anhydrous (97% Strem Chemicals), bis(triphenylphosphine)palladium(II) dichloride (96%, Oakwood Chemical), sodium carbonate (ACS grade, Ameresco), magnesium sulfate anhydrous (99.4%, Chem-Impex, International Inc.), sodium sulfate anhydrous (99.5%, Oakwood Chemical), sodium chloride (ACS grade, Fisher Chemical), sodium hydroxide (ACS, Oakwood Chemical), potassium hydroxide (ACS grade, Fisher Chemical), potassium carbonate (99.8%, Mallinckrodt), sodium nitrite (98%, Oakwood Chemical), silica gel (60 nm, Macron), 1,3,3-trimethylindolino-6'-nitrobenzopyrylospiran (98%, TCI), 2,5-dibromonitrobenzene (99%, Oakwood Chemical), 3-methyl-2-butanone (>99%, TCI), methyl trifluoromethanesulfonate (97%, Matrix Scientific), 2-hydroxy-5-nitrobenzaldehyde (98%, Oakwood Chemical), 1,3,5-tribromobenzene (98%, Sigma-Aldrich), 1,4-dimethoxybenzene (99%, Oakwood Chemical), 4-aminophenylboronic acid

hydrochloride (99%, Chem-Impex International, Inc.), Aliquat 336 (reagent grade, BeanTown Chemical), boron tribromide (reagent grade, Sigma-Aldrich), propargyl bromide (80 wt. % in toluene, reagent grade, Oakwood Chemical), *n*-butyllithium (reagent grade, Sigma-Aldrich), hydrochloric acid (ACS, Fisher Chemical), sulfuric acid (ACS grade, Fisher Chemical), nitric acid (ACS reagent, Sigma-Aldrich), fluoroboric acid (48%, Oakwood Chemical), acetic acid (ACS grade, Fisher Chemical), ethanol (200 proof, Decon Laboratories, Inc.), methanol (ACS grade, Fisher Chemical), acetone (ACS grade, Sigma-Aldrich), ethyl acetate (99.9%, Fisher Chemical), chloroform (99.9%, Fisher Chemical), dichloromethane (ACS grade, Macron), diethyl ether (ACS grade, J. T. Baker® Chemicals), hexanes (ACS grade, BDH), acetonitrile (ACS grade, Fisher), *N*,*N*-dimethylformamide (ACS grade, Oakwood Chemical), *N,N*-diethylformamide (>99%, TCI), piperidine (99%, Sigma-Aldrich), carbon tetrachloride (99.9%, Sigma-Aldrich), bromine (99.8%, Acros Organics), tetrahydrofuran (HPLC grade, BeanTown Chemical), 1-butanol (99.4%, Oakwood Chemical), 1,2-dichlorobenzene (98%, Alfa Aesar), 1,4-dioxane (99+%, Alfa Aesar), chloroform-*d* (Cambridge Isotope Laboratories, Inc.), deuterium chloride (Sigma-Aldrich), and dimethyl sulfoxide-d_6 (Cambridge Isotope Laboratories, Inc.) were used as received.

The MOF and COF linkers, 1',3',3'-trimethyl-6-nitro-4',7'-di(pyridin-4-yl)spiro[chromene-2,2'-indoline] (TNDS),[42] 3',6'-dibromo-4',5'-bis(4-carboxyphenyl)-[1,1':2',1''-terphenyl]-4,4''-dicarboxylic acid (H_4DBTD),[68] 2,5-dimethoxyterephthalaldehyde (DMTA),[69] 1,3,5-tri-(4-aminophenyl)benzene (TAPB),[70] and 2,5-bis(2-propynyloxy)terephthalaldehyde (BPTA),[71] were synthesized based on modified literature procedures. The MOFs, Zn_2(ZnTCPP)[50] and Zn_2(DBTD)(TNDS),[42] were synthesized based on modified literature procedures. The COFs, COF**1**[66,67] and SP@COF**1**,[44] were synthesized based on modified literature procedures.

Preparation of Zn_2(ZnTCPP)(TNDS)

The MOF, Zn_2(TNDS)(ZnTCPP), was prepared using a modified literature procedure.[50] In a one-dram vial, $Zn(NO_3)_2 \cdot 6H_2O$ (17 mg, 57 μmol) and H_4TCPP (7.9 mg, 0.010 mmol) were dissolved in 2.1/0.5 mL DEF/EtOH followed by sonication for 10 min. To the solution, TNDS (7.2 mg, 0.015 mmol) in 0.16 mL DEF (*N,N*-diethylformamide) and 30 μL of HNO_3 (1.0 M in ethanol (EtOH)) were added. The resulting solution was sonicated for 10 min and then heated at 80 °C for 14 hr in an isothermal oven. After heating for 14 hr, the reaction mixture was cooled down to room temperature over 2 hr. Dark red plate-like crystals of Zn_2(ZnTCPP)(TNDS) (15 mg, 9.2 μmol) were isolated in 92% yield. FTIR (neat, cm^{-1}): 660, 665, 701, 713, 718, 735, 747, 775, 794, 838, 872, 888, 996, 1010, 1022, 1063, 1100, 1143, 1175, 1204, 1255, 1277, 1338, 1387, 1398, 1492, 1504, 1550, 1603, 1618, 1649, 1656, and 2927 (Figure S3). The PXRD pattern of Zn_2(ZnTCPP)(TNDS) is shown in Figure S2. The ^{1}H NMR spectrum and MS data of digested Zn_2(ZnTCPP)(TNDS) are shown in Figure S4. The experimental procedure utilized for MOF digestion can be found below.

Preparation of SP@COF1

The COF, SP@COF**1**, was prepared using a modified literature procedure.[44] In a one-dram vial, COF**1** (18.0 mg) and 1,3,3-trimethylindolino-6'-nitrobenzopyrylospiran (SP; 64.0 mg, 0.198 mmol) were added, followed by the addition of THF (0.400 mL) and heated at 40 °C. After 72 hr, the precipitate was collected and washed with THF (5 mL) and acetonitrile (5 mL) to remove any excess SP from the surface of the COF. As a result, a yellow powder (16 mg) was collected. FTIR (neat, cm^{-1}): 662, 694, 739, 828, 879, 1014, 1038, 1095, 1144, 1180, 1210, 1289, 1340, 1409, 1443, 1464, 1489, 1504, 1591, 1611, 1673, 1717, 1727, 2044, 2854, 2924, and 2960

(Figure S8). The PXRD pattern of SP@COF**1** is shown in Figure S7. The ^{1}H NMR spectrum of digested SP@COF**1** is shown in Figure S9. It was determined to have 0.46 SP per three –OMe units (i.e., 0.46 SP per COF pore). The experimental procedure utilized for COF digestion can be found below.

General digestion procedure

In order to study the prepared MOFs and COFs by ^{1}H NMR spectroscopy, a solution of 500 µL of DMSO-d_6 and 5.0 µL of deuterium chloride were added to 5.0 mg of washed material, followed by sonication for five min and heating at 75 °C (MOFs) or 100 °C (COFs) for 24 hr. The percentage of each component were calculated based on proton ratios found through integration of signals in the ^{1}H NMR spectra of digested samples (Figure S4 and S9).

Diffuse reflectance and photoluminescence spectroscopy

Diffuse reflectance spectra were collected on an Ocean Optics JAZ spectrometer. An Ocean Optics ISP-REF integrating sphere was connected to the spectrometer using a 450 µm SMA fiber optic cable. Samples were loaded in a 4.0 mm quartz sample cell, which was referenced to an Ocean Optics WS-1 Spectralon® standard. A mounted high-powered LED (M365L2, Thorlabs, λ_{ex} = 365 nm, distance = 1 cm, LEDD1B power supply set at 700 mA) was used for *in situ* irradiation of the samples.

Steady-state emission spectra were acquired on an Edinburgh FS5 fluorescence spectrometer equipped with a 150 W Continuous Wave Xenon Lamp source for excitation. Emission measurements on solid samples were collected on the powders of the desired materials placed inside a 0.5 mm quartz sample holder using the front-facing module.

Emission via epifluorescence microscopy was measured using an Olympus BX51 microscope equipped with a UV filter cube that allows excitation between 330–385 nm and emission from >420 nm (Olympus U-MWU2). A 120 W mercury vapor short arc lamp was used as an excitation light source. Samples were measured under simultaneous irradiation until no changes in emission were observed for 30 s. For measurements over time, spectra were recorded on an Ocean Optics USB4000 spectrometer under continuous UV-irradiation (λ_{ex} = 330–385 nm) and the epifluorescence microscopic images of samples before and after UV-irradiation were collected with a color digital CMOS camera (Canon EOS REBEL T3/1100D). The integration time was set to 100 ms with 10 scans averaged per spectrum and a boxcar width of 5.

Fluorescence decay lifetimes were measured using a DeltaFlex TCSCP Lifetime Fluorometer from Horiba Instruments equipped with a 373-nm pulsed-laser diode. First, a small spot of type-NVH immersion oil (Cargille Labs) was placed onto the polished side of a cut silicon wafer and then the sample was mixed with the immersion oil. The silicon wafer was then placed on the front-facing module. Prior to reaching the photon counter, light passed through a monochromator set to 660 nm to filter stray light. MOFs were irradiated for five min (ten min for COFs) with UV light prior to sample measurement to ensure conversion to merocyanine.

Optical Cycling

Optical cycling of photochromic MOFs and COFs was carried out using an Ocean Optics JAZ spectrometer. An Ocean Optics ICPREF integration sphere was connected to the spectrometer using a 450-µm SMA fiber optic cable. Prior to time-resolved DR measurements, the sample background spectrum was subtracted to remove the region that does not

correspond to photophysical behavior of the photochromic moieties integrated into the framework. A sample was placed inside a 4.0-mm quartz sample holder and a 400-nm longpass glass filter (Thorlabs, FGCL400) was placed between the quartz sample cell with a quartz cover slide and the integrating sphere to filter any UV light from the internal tungsten-halogen lamp. The quartz sample holder with a quartz cover slide and longpass filter were attached to the top of the integrating sphere with electrical tape to prevent sample displacement. A mounted high-powered LED (M365L2, Thorlabs, λ_{ex} = 365 nm, distance = 2 cm, and LEDD1B power supply set to 245 mA) was used for *in situ* irradiation of the sample for 1 min, then the sample was allowed to undergo photoinduced reversion on the top of the integration sphere for 15 s while a spectrum was collected every 200 ms. This procedure was repeated for three consecutive irradiation cycles (Figure 2).

Conductivity measurements

A two-point method was employed to measure conductivity, σ (S/cm), of pressed pellets according to the following equation:

$$\sigma = Il/VA,$$

Where I = current, l = thickness of the pellets, V = voltage, and A = surface area of the prepared pellets.

The electrical conductance in the prepared materials followed Ohm's law and was measured by fitting a linear current (I)-voltage (V) curve. An "in-house" two-contact probe pressed pellet setup (2C3PS)[60,72,73] made it possible to fabricate the pressed pellets and perform measurements *in situ* while also allowing for simultaneous MOF irradiation and monitoring changes in electrical current flow under applied voltage. The MOF powder (10 mg), pre-dried for 20 min in air (unless otherwise noted), was pressed between two stainless steel rods inside an insulating quartz tube. The diameter of the resulting pellet was the same as the inner diameter of the quartz tube (d = 2 mm). The thickness of the pellets was kept consistent (l = 1 mm) by using the same amount of material. After forming a small pellet, the stainless-steel rods were connected to a sourcemeter (Keithley Instruments GmbH, Germering, Germany, model 2636A) using a 3-slot triax-to-alligator clip cable to perform conductivity measurements. For all measurements, the number of power line cycles (NPLC) was set to 5 with a delay of 1 ms.

To measure the electrical conductivity for photochromic MOFs before and after irradiation with UV light, the samples were first dried in air for 20 min and then placed into the 2C3PS. The samples were measured in the dark initially and then again after irradiation with a mounted high-powered LED (M365L2, Thorlabs, λ_{ex} = 365 nm, distance = 6 cm, LEDD1B power supply set at 700 mA) for 5 min. The measurements were performed using the 2C3PS connected to a sourcemeter (Keithley Instruments GmbH, Germering, Germany, model 2636A). The I–V curves were collected by supplying a voltage in the range from −1 V to +1 V. The electrical conductance in the prepared materials follows Ohm's law and was estimated by fitting the obtained linear I–V curves.

Conductance cycling

Dependence of the current values on UV- and visible-light excitation wavelength for Zn_2(ZnTCPP)(TNDS) was measured in the previously discussed 2C3PS that was connected to a sourcemeter (Keithley Instruments GmbH, Germering, Germany, model 2636A; Figure 2). A constant voltage (500 mV) was applied while current was measured every 100 ms (NPLC = 5

with a delay of 1 ms). Before data collection, an equilibration time (t = 90 s) was applied in the dark. Then, the sample was irradiated (t = 15 s) using a high-powered LED (M365L2, Thorlabs λ_{ex} 365 nm, the LED-sample distance = 2 cm, LEDD1B power supply set to 700 mA), followed by thermal relaxation in the dark (t = 15 s). The procedure was repeated for three consecutive irradiation cycles. PXRD studies were used to confirm the integrity of the MOFs and COFs after optical cycling (Figure S12–S14).

Other physical measurements

FTIR spectra were obtained on a Perkin-Elmer Spectrum 100. ^{1}H NMR spectra were collected on a Bruker Avance III-HD 400 MHz NMR spectrometer. ^{1}H NMR spectra were referenced to residual ^{1}H peaks of deuterated solvents. PXRD patterns of MOFs were recorded on a Rigaku Miniflex 6G diffractometer at a scan rate of 10 °/min with accelerating voltage and current of 40 kV and 15 mA, respectively. PXRD patterns of COFs were recorded on a Rigaku Miniflex 6G diffractometer at a scan rate of 5 °/min with accelerating voltage and current of 40 kV and 15 mA, respectively. The Water QTOF-I quadrupole time-of-flight and Thermo Scientific Orbitrap Velos Pro mass spectrometers were used to record the mass spectra of the prepared compounds.

Conflicts of interest

There are no conflicts to declare.

Acknowledgements

This work was supported by the NSF CAREER Award (DMR-1553634). This work was also supported by the Cottrell Scholar Award from the Research Corporation for Science Advancement, Camille Dreyfus Teaching-Scholar Award provided by Henry and Camille Dreyfus Foundation, and the Hans Fischer Fellowship.

Notes and references

1 I. Hod, M. D. Sampson, P. Deria, C. P. Kubiak, O. K. Farha and J. T. Hupp, *ACS Catal.*, 2015, **5**, 6302–6309.

2 C. S. Diercks, S. Lin, N. Kornienko, E. A. Kapustin, E. M. Nichols, C. Zhu, Y. Zhao, C. J. Chang and O. M. Yaghi, *J. Am. Chem. Soc.*, 2018, **140**, 1116–1122.

3 N. Kornienko, Y. Zhao, C. S. Kley, C. Zhu, D. Kim, S. Lin, C. J. Chang, O. M. Yaghi and P. Yang, *J. Am. Chem. Soc.*, 2015, **137**, 14129–14135.

4 T. Simon-Yarza, A. Mielcarek, P. Couvreur and C. Serre, *Adv. Mater.*, 2018, **30**, 1707365.

5 A. Das and D. M. D'Alessandro, *Dalton Trans.*, 2016, **45**, 6824–6829.

6 Y. Takashima, V. M. Martínez, S. Furukawa, M. Kondo, S. Shimomura, H. Uehara, M. Nakahama, K. Sugimoto and S. Kitagawa, *Nat. Commun.*, 2011, **2**, 168.

7 S.-Y. Zhang, W. Shi, P. Cheng and M. J. Zaworotko, *J. Am. Chem. Soc.*, 2015, **137**, 12203–

12206.

8 F.-X. Coudert and A. H. Fuchs, *Coord. Chem. Rev.*, 2016, **307**, 211–236.

9 C. Orellana-Tavra, S. A. Mercado and D. Fairen-Jimenez, *Adv. Healthc. Mater.*, 2016, **5**, 2261–2270.

10 K. M. Choi, D. Kim, B. Rungtaweevoranit, C. A. Trickett, J. T. D. Barmanbek, A. S. Alshammari, P. Yang and O. M. Yaghi, *J. Am. Chem. Soc.*, 2017, **139**, 356–362.

11 H.-C. Zhou and S. Kitagawa, *Chem. Soc. Rev.*, 2014, **43**, 5415–5418.

12 X. Kang, X. Wu, X. Han, C. Yuan, Y. Liu and Y. Cui, *Chem. Sci.*, 2020, **11**, 1494–1502.

13 S. Rojas, A. Arenas-Vivo and P. Horcajada, *Coord. Chem. Rev.*, 2019, **388**, 202–226.

14 Y. Zhang, J. Pang, J. Li, X. Yang, M. Feng, P. Cai and H.-C. Zhou, *Chem. Sci.*, 2019, **10**, 8455–8460.

15 W. Hu, F. Yang, N. Pietraszak, J. Gu and J. Huang, *Phys. Chem. Chem. Phys.*, 2020, **22**, 25445–25449.

16 M. A. Gerkman, R. S. L. Gibson, J. Calbo, Y. Shi, M. J. Fuchter and G. G. D. Han, *J. Am. Chem. Soc.*, 2020, **142**, 8688–8695.

17 N. D. Rudd, Y. Liu, K. Tan, F. Chen, Y. J. Chabal and J. Li, *ACS Sustain. Chem. Eng.*, 2019, **7**, 6561–6568.

18 Y. Chen, P. Li, J. Zhou, C. T. Buru, L. Đorđević, P. Li, X. Zhang, M. M. Cetin, J. F. Stoddart, S. I. Stupp, M. R. Wasielewski and O. K. Farha, *J. Am. Chem. Soc.*, 2020, **142**, 1768–1773.

19 W. Jiao, J. Zhu, Y. Ling, M. Deng, Y. Zhou and P. Feng, *Nanoscale*, 2018, **10**, 20339–20346.

20 M. Kalaj and S. M. Cohen, *ACS Cent. Sci.*, 2020, **6**, 1046–1057.

21 W. Zhou, D.-D. Huang, Y.-P. Wu, J. Zhao, T. Wu, J. Zhang, D.-S. Li, C. Sun, P. Feng and X. Bu, *Angew. Chem. Int. Ed.*, 2019, **58**, 4227–4231.

22 M. B. Majewski, A. W. Peters, M. R. Wasielewski, J. T. Hupp and O. K. Farha, *ACS Energy Lett.*, 2018, **3**, 598–611.

23 F. Bigdeli, C. T. Lollar, A. Morsali and H.-C. Zhou, *Angew. Chem. Int. Ed.*, 2020, **59**, 4652–4669.

24 Z. Xia, F. Li, L. Xu and P. Feng, *Dalton Trans.*, 2020, **49**, 11157–11162.

25 X.-Y. Liu, W. P. Lustig and J. Li, *ACS Energy Lett.*, 2020, **5**, 2671–2680.

26 R. C. e Silva, L. O. da Silva, A. de Andrade Bartolomeu, T. J. Brocksom and K. T. de Oliveira, *Beilstein J. Org. Chem.*, 2020, **16**, 917–955.

27 D. E. Williams and N. B. Shustova, *Chem. Eur. J.*, 2015, **21**, 15474–15479.

28 M. C. So, G. P. Wiederrecht, J. E. Mondloch, J. T. Hupp and O. K. Farha, *Chem. Commun.*, 2015, **51**, 3501–3510.

29 E. A. Dolgopolova, A. M. Rice, M. D. Smith and N. B. Shustova, *Inorg. Chem.*, 2016, **55**, 7257–

7264.

30 E. A. Dolgopolova, D. E. Williams, A. B. Greytak, A. M. Rice, M. D. Smith, J. A. Krause and N. B. Shustova, *Angew. Chem. Int. Ed.*, 2015, **54**, 13639–13643.

31 J. Park, D. Feng, S. Yuan and H.-C. Zhou, *Angew. Chem. Int. Ed.*, 2015, **54**, 430–435.

32 D. E. Williams, J. A. Rietman, J. M. Maier, R. Tan, A. B. Greytak, M. D. Smith, J. A. Krause and N. B. Shustova, *J. Am. Chem. Soc.*, 2014, **136**, 11886–11889.

33 C. Y. Lee, O. K. Farha, B. J. Hong, A. A. Sarjeant, S. T. Nguyen and J. T. Hupp, *J. Am. Chem. Soc.*, 2011, **133**, 15858–15861.

34 K. C. Park, C. Seo, G. Gupta, J. Kim and C. Y. Lee, *ACS Appl. Mater. Interfaces*, 2017, **9**, 38670–38677.

35 Q. Zhang, C. Zhang, L. Cao, Z. Wang, B. An, Z. Lin, R. Huang, Z. Zhang, C. Wang and W. Lin, *J. Am. Chem. Soc.*, 2016, **138**, 5308–5315.

36 S.-Y. Ding, P.-L. Wang, G.-L. Yin, X. Zhang and G. Lu, *Int. J. Hydrogen Energy*, 2019, **44**, 11872–11876.

37 L. Yao, Y. Zhang, H.-X. Wang, Y. Guo, Z.-M. Zhuang, W. Wen, X. Zhang and S. Wang, *J. Mater. Chem. A*, 2020, **8**, 8518–8526.

38 A. M. Rice, C. R. Martin, V. A. Galitskiy, A. A. Berseneva, G. A. Leith and N. B. Shustova, *Chem. Rev.*, 2020, **120**, 8790–8813.

39 A. Gonzalez, E. S. Kengmana, M. V. Fonseca and G. G. D. Han, *Mater. Today Adv.*, 2020, **6**, 100058.

40 R. Klajn, *Chem. Soc. Rev.*, 2014, **43**, 148–184.

41 K. Healey, W. Liang, P. D. Southon, T. L. Church and D. M. D'Alessandro, *J. Mater. Chem. A*, 2016, **4**, 10816–10819.

42 D. E. Williams, C. R. Martin, E. A. Dolgopolova, A. Swifton, D. C. Godfrey, O. A. Ejegbavwo, P. J. Pellechia, M. D. Smith and N. B. Shustova, *J. Am. Chem. Soc.*, 2018, **140**, 7611–7622.

43 C. R. Martin, G. A. Leith, P. Kittikhunnatham, K. C. Park, O. A. Ejegbavwo, A. Mathur, C. R. Callahan, S. L. Desmond, M. R. Keener, F. Ahmed, S. Pandey, M. D. Smith, S. R. Phillpot, A. B. Greytak and N. B. Shustova, *Angew. Chem. Int. Ed.*, 2021, **133**, 8152–8160.

44 S. Garg, H. Schwartz, M. Kozlowska, A. B. Kanj, K. Müller, W. Wenzel, U. Ruschewitz and L. Heinke, *Angew. Chem. Int. Ed.*, 2019, **58**, 1193–1197.

45 M. Irie, T. Fukaminato, K. Matsuda and S. Kobatake, *Chem. Rev.*, 2014, **114**, 12174–12277.

46 M. Irie, *Chem. Rev.*, 2000, **100**, 1685–1716.

47 D. G. Patel, I. M. Walton, J. M. Cox, C. J. Gleason, D. R. Butzer and J. B. Benedict, *Chem. Commun.*, 2014, **50**, 2653–2656.

48 I. M. Walton, J. M. Cox, T. B. Mitchell, N. P. Bizier and J. B. Benedict, *CrystEngComm*, 2016, **18**, 7972–7977.

49 I. M. Walton, J. M. Cox, C. A. Benson, D. G. Patel, Y.-S. Chen and J. B. Benedict, *New J. Chem.*, 2016, **40**, 101–106.

50 E.-Y. Choi, C. A. Wray, C. Hu and W. Choe, *CrystEngComm*, 2009, **11**, 553–555.

51 B. J. Burnett and W. Choe, *CrystEngComm*, 2012, **14**, 6129–6131.

52 B. J. Burnett, P. M. Barron, C. Hu and W. Choe, *J. Am. Chem. Soc.*, 2011, **133**, 9984–9987.

53 K. Kruttwig, D. R. Yankelevich, C. Brueggemann, C. Tu, N. L'Etoile, A. Knoesen and A. Y. Louie, *Molecules*, 2012, **17**, 6605–6624.

54 S. Scarmagnani, Z. Walsh, C. Slater, N. Alhashimy, B. Paull, M. Macka and D. Diamond, *J. Mater. Chem.*, 2008, **18**, 5063–5071.

55 A. Barroso-Bogeat, M. Alexandre-Franco, C. Fernández-González and V. Gómez-Serrano, *Energy Fuels*, 2014, **28**, 4096–4103.

56 J. Buback, P. Nuernberger, M. Kullmann, F. Langhojer, R. Schmidt, F. Würthner and T. Brixner, *J. Phys. Chem. A*, 2011, **115**, 3924–3935.

57 E. A. Dolgopolova, A. M. Rice, C. R. Martin and N. B. Shustova, *Chem. Soc. Rev.*, 2018, **47**, 4710–4728.

58 D. Kim, Z. Zhang and K. Xu, *J. Am. Chem. Soc.*, 2017, **139**, 9447–9450.

59 M. Sanchez-Lozano, C. M. Estévez, J. Hermida-Ramón and L. Serrano-Andres, *J. Phys. Chem. A*, 2011, **115**, 9128–9138.

60 E. A. Dolgopolova, V. A. Galitskiy, C. R. Martin, H. N. Gregory, B. J. Yarbrough, A. M. Rice, A. A. Berseneva, O. A. Ejegbavwo, K. S. Stephenson, P. Kittikhunnatham, S. G. Karakalos, M. D. Smith, A. B. Greytak, S. Garashchuk and N. B. Shustova, *J. Am. Chem. Soc.*, 2019, **141**, 5350–5358.

61 C. F. Leong, C.-H. Wang, C. D. Ling and D. M. D'Alessandro, *Polyhedron*, 2018, **154**, 334–342.

62 H. L. Nguyen, T. T. Vu, D. Le, T. L. H. Doan, V. Q. Nguyen and N. T. S. Phan, *ACS Catal.*, 2017, **7**, 338–342.

63 K. Geng, T. He, R. Liu, S. Dalapati, K. T. Tan, Z. Li, S. Tao, Y. Gong, Q. Jiang and D. Jiang, *Chem. Rev.*, 2020, **120**, 8814–8933.

64 M. S. Lohse and T. Bein, *Adv. Funct. Mater.*, 2018, **28**, 1705553.

65 G. A. Leith, A. A. Berseneva, A. Mathur, K. C. Park and N. B. Shustova, *Trends Chem.*, 2020, **2**, 367–382.

66 H. Xu, J. Gao and D. Jiang, *Nat. Chem.*, 2015, **7**, 905–912.

67 A. M. Rice, E. A. Dolgopolova, B. J. Yarbrough, G. A. Leith, C. R. Martin, K. S. Stephenson, R. A. Heugh, A. J. Brandt, D. A. Chen, S. G. Karakalos, M. D. Smith, K. B. Hatzell, P. J. Pellechia, S. Garashchuk and N. B. Shustova, *Angew. Chem. Int. Ed.*, 2018, **57**, 11310–11315.

68 O. K. Farha, C. D. Malliakas, M. G. Kanatzidis and J. T. Hupp, *J. Am. Chem. Soc.*, 2010, **132**, 950–952.

69 J.-I. Kadokawa, Y. Tanaka, Y. Yamashita and K. Yamamoto, *Eur. Polym. J.*, 2012, **48**, 549–559.

70 M. G. Schwab, M. Hamburger, X. Feng, J. Shu, H. W. Spiess, X. Wang, M. Antonietti and K. Müllen, *Chem. Commun.*, 2010, **46**, 8932–8934.

71 S. Jeon, S. Park, J. Nam, Y. Kang and J.-M. Kim, *ACS Appl. Mater. Interfaces*, 2016, **8**, 1813–1818.

72 L. Sun, S. S. Park, D. Sheberla and M. Dincă, *J. Am. Chem. Soc.*, 2016, **138**, 14772–14782.

73 F. Wudl and M. R. Bryce, *J. Chem. Educ.*, 1990, **67**, 717–718.